



Relationships between HI Gas Mass, Stellar Mass, and the Star Formation Rate of HICAT+WISE (HI-WISE) Galaxies

Vaishali Parkash¹ , Michael J. I. Brown¹ , T. H. Jarrett² , and Nicolas J. Bonne³

¹ School of Physics and Astronomy, Monash Centre for Astrophysics (MoCA), Monash University, Clayton, Victoria 3800, Australia; vaishali.parkash@monash.edu

² Astrophysics, Cosmology and Gravity Centre (ACGC), Astronomy Department, University of Cape Town, Private Bag X3, Rondebosch 7701, South Africa

³ Institute for Cosmology and Gravitation, Dennis Sciama Building, University of Portsmouth, Burnaby Road, Portsmouth PO1 3FX, UK

Received 2017 October 1; revised 2018 June 3; accepted 2018 June 29; published 2018 August 29

Abstract

We have measured the relationships between HI mass, stellar mass, and star formation rate using the HI Parkes All-Sky Survey Catalog (HICAT) and the *Wide-field Infrared Survey Explorer* (WISE). Of the 3513 HICAT sources, we find 3.4 μm counterparts for 2896 sources (80%), and provide new WISE-matched aperture photometry for these galaxies. For our principal sample of spiral galaxies with $W1 \leq 10$ mag and $z \leq 0.01$, we identify HI detections for 93% of the sample. We measure lower HI–stellar mass relationships for HI-selected samples that do not include spiral galaxies with little HI gas. Our observations of the spiral sample show that HI mass increases with stellar mass with a power-law index of 0.35; however, this value is dependent on T-type, which affects both the median and the dispersion of HI mass. We also observe an upper limit on the HI gas fraction, which is consistent with a halo spin parameter model. We measure the star formation efficiency of spiral galaxies to be constant at $10^{-9.57} \text{ yr}^{-1} \pm 0.4$ dex for 2.5 orders of magnitude in stellar mass, despite the higher stellar mass spiral showing evidence of quenched star formation.

Key words: galaxies: evolution – galaxies: fundamental parameters – galaxies: spiral – galaxies: star formation – radio lines: galaxies – radio lines: ISM

Supporting material: machine-readable table

1. Introduction

Star formation is fueled by atomic (HI) and molecular hydrogen, so we expect correlations between HI mass, stellar mass, and star formation rates (SFRs). This is exemplified by the Kennicutt–Schmidt law, which establishes a correlation between gas surface density and SFR, albeit both for HI and molecular gas, and with considerable scatter (Kennicutt 1998). Correlations are also observed between stellar mass and HI mass (e.g., Catinella et al. 2010; Huang et al. 2012; Maddox et al. 2015), although these are partially explained by luminosity–luminosity correlations. However, the presence of mass quenching indicates that HI mass declines above some high stellar mass threshold (e.g., Kauffmann et al. 2003; Gabor et al. 2010).

Although the relationship between HI mass and SFR in a galaxy is predicted by the Kennicutt–Schmidt law, there is a scatter of ~ 0.2 dex (Kennicutt 1998), implying that HI mass is just one of several factors that regulate SFR. Multiple studies using different surveys find that HI mass (M_{HI}) increases with SFR (Mirabel & Sanders 1988; Doyle & Drinkwater 2006). A HI disk is a precondition for star formation, but star formation also requires gas accretion from the intergalactic medium to drive the HI gas inward, thereby cooling and converting it into molecular hydrogen (e.g., Prochaska & Wolfe 2009; Obreschkow et al. 2016). By comparison, the relationship between molecular hydrogen and SFR is better understood since stars form in molecular clouds. Recent works (Leroy et al. 2008; Schruba et al. 2011) have shown that molecular hydrogen, rather than HI, drives the Kennicutt–Schmidt law, but an empirical study on the relationship between molecular hydrogen and SFR using a large sample of galaxies is difficult to perform because of the lack of large-scale CO surveys. Also, there is uncertainty in converting CO intensity to molecular

hydrogen content due to the uncertainty in the X-factor (Bolatto et al. 2013). Although HI gas is only indirectly related to the SFR, the results of measurements of HI gas can be used to imply information about the molecular hydrogen of a galaxy (e.g., Leroy et al. 2008; Wong et al. 2016).

Multiple studies have found that HI mass increases with stellar mass (Catinella et al. 2010; Huang et al. 2012; Maddox et al. 2015), which is partially explained by luminosity–luminosity correlations. However, the relations measured by different studies disagree with each other. Huang et al. (2012) found $\langle \log M_{\text{HI}} \rangle \propto 0.712 \langle \log M_* \rangle$ for $M_* \leq 10^9 M_\odot$ and $\langle \log M_{\text{HI}} \rangle \propto 0.276 \langle \log M_* \rangle$ for $M_* > 10^9 M_\odot$. The break in the relationship represents the transition from irregular, low stellar mass galaxies to high mass, disk galaxies (Kereš et al. 2009; Maddox et al. 2015). However, Catinella et al. (2010) observed that HI mass increases only slightly with stellar mass (to the power of 0.02) for galaxies with $M_* > 10^9 M_\odot$.

The differences in the relation between HI mass and stellar mass in the literature may be due to sample selection. The samples of Huang et al. (2012) and Maddox et al. (2015) use the HI Arecibo Legacy Fast ALFA (ALFALFA) survey population, while the GASS sample of Catinella et al. (2010) is selected by stellar mass ($M_* > 10^{10} M_\odot$). By definition, the HI-selected samples of Huang et al. (2012) and Maddox et al. (2015) are more HI-rich compared to stellar mass-selected samples, and are biased against high stellar mass elliptical galaxies with very little HI gas, resulting in elevated trends for HI mass versus stellar masses. While the literature shows that HI mass increases with stellar mass, perhaps with a break or a plateau at high stellar masses (i.e., Catinella et al. 2010; Huang et al. 2012; Maddox et al. 2015), there are quantitative disagreements that we suspect are the result of sample selections.

How the HI-based star formation efficiency (SFE), or its inverse, the HI-depletion timescale (t_{dep}), varies with a galaxy’s stellar mass is unclear from the current literature. Huang et al. (2012), Jaskot et al. (2015), and Lutz et al. (2017) found that SFE increases with stellar mass for HI-selected samples. Therefore, low mass galaxies that are more HI-rich than high stellar mass galaxies are inefficient at using their fuel reservoirs to form stars. Contradicting this, Schiminovich et al. (2010) found the SFE of massive galaxies ($M_* > 10^{10} M_\odot$) to be constant at $10^{-9.5} \text{ yr}^{-1}$, and Wong et al. (2016) found SFE to be constant at $10^{-9.65} \text{ yr}^{-1}$ across five orders of magnitude of stellar mass for star-forming galaxies. Incompleteness and sample size are issues for relations from the prior literature, with Jaskot et al. (2015) having *Wide-field Infrared Survey Explorer* (*WISE*) detections for 63% of their HI sources, while Wong et al. (2016) is highly complete, containing just 84 galaxies.

A key limitation of previous studies is low completeness, particularly for infrared counterparts for HI sources, which facilitate the measurement of stellar masses and SFRs. Doyle & Drinkwater (2006) used fluxes from the *Infrared Astronomical Satellite* (*IRAS*) to calculate SFRs for galaxies in the HI Parkes All-Sky Survey (HIPASS) optical catalog (HOPCAT) (Doyle et al. 2005). Due to the 0.5’ angular resolution and 0.7 Jy 10σ sensitivity of the *IRAS* at 12 μm , they only found infrared counterparts for 32% of the HIPASS catalog (HICAT). Their final sample comprised galaxies with high SFRs and excluded galaxies with low rates of star formation, including elliptical galaxies and dwarf galaxies, because at $z = 0.01$ the *IRAS* can only detect sources brighter than $\nu L_\nu \sim 1 \times 10^{10} L_\odot$. Jaskot et al. (2015) improved previous studies by using *WISE*, which has a 12 μm 5σ sensitivity of 1 mJy, but at the $z \sim 0.06$ maximum redshift of ALFALFA galaxies *WISE* detects galaxies brighter than $\nu L_\nu \sim 6 \times 10^8 L_\odot$, which resulted in Jaskot et al. (2015) finding infrared counterparts for just 63% of their HI sources. To improve on the prior literature, we need large samples of galaxies that are highly complete for HI counterparts, while probing large ranges of stellar mass, HI mass, and SFR.

For this work, we measure the relationship between HI mass, stellar mass, and SFR using three galaxy samples combining HICAT and *WISE*. The paper is arranged as follows: Section 2 describes the data used in this research; Section 3 details the equations used to calculate the masses and SFRs; Section 4 describes the samples; Sections 5 and 6 present the results; Section 7 discusses the results; and Section 8 summarizes our work. All magnitudes are in the Vega system. The cosmology applied in this paper is $H_0 = 70 \text{ km s}^{-1}$, $\Omega_M = 0.3$, and $\Omega_\Lambda = 0.7$.

2. Data

2.1. HICAT

The principal source of data for our analysis is HICAT, which is derived from HIPASS (Barnes et al. 2001; Meyer et al. 2004). HIPASS is a blind survey below a declination δ of $+2^\circ$, performed with the Parkes 64 m radio telescope using a 21 cm multibeam receiver. HICAT contains 4315 HI sources selected from HIPASS and is 99% complete at a peak flux of 84 mJy and an integrated flux of 9.4 Jy km s^{-1} (Meyer et al. 2004; Zwaan et al. 2004).

Table 1
The Number of Optical Matches for HICAT

	Number of Sources
Total	4315
No optical match	596
Position and velocity match	3313
Position match	406
Bonne et al. (2015)	1043
NED and HYPERLEDA	2270
HOPCAT	406

For each HI source in HICAT, we search for optical counterparts using the position and velocity measurements in HICAT. Since the HIPASS data has a spatial resolution of 15.5’, it is necessary to obtain more accurate positions for the HI sources before searching for their mid-infrared counterparts in the *WISE* frames. To this end, we search for optical counterparts in the spectroscopic sample of Bonne et al. (2015), the NASA/IPAC Extragalactic Database (NED),⁴ HYPERLEDA (Makarov et al. 2014), and HOPCAT (Doyle et al. 2005). In order to accurately match the HI sources with their optical counterparts, we cross-check the velocity measurements from HICAT with the velocity provided from the above sources for all possible positional matches. We describe each source below—as well as the matching process—in detail.

In our preliminary search for optical counterparts, we use the spectroscopic sample of Bonne et al. (2015), which covers the full survey area of HICAT and provides velocities (predominantly from the $r_F \leq 15.60$ 2MASS selected 6dF Galaxy Survey, 6dFGS; Jones et al. 2009), morphologies, and *WISE* photometry from the All-Sky public-release archive (Cutri et al. 2013a) for 13325 galaxies. For each source, we select the best match to this sample within 5’ and 400 km s^{-1} of the respective HICAT position and velocity, resulting in 1043 optical counterparts of 4315 HI sources.

To obtain additional optical counterparts, we then search in NED and HYPERLEDA for galaxies within 10’ and 400 km s^{-1} of their respective HICAT positions and velocities. As NED and HYPERLEDA draw information from catalogs such as HICAT, it must be ensured that the velocities extracted from these databases are sourced from optical or high-resolution HI radio observations and not sourced from HICAT, and hence that HICAT velocities are not being cross-matched to themselves.

HOPCAT (Doyle et al. 2005) is used as our last source for optical matches. The matches from HOPCAT cannot be cross-checked with known velocities, but are categorized as “good guesses” by Doyle et al. (2005; see the reference for details on HOPCAT and its matching criteria). We do not use HOPCAT as our primary source for optical matches because Bonne et al. (2015), NED, and HYPERLEDA described above provide more recent velocity measurements from 6dFGS and other surveys that were not available at the time HOPCAT was compiled. The final number of galaxies taken from each source described here is listed in Table 1. In total, optical counterparts were obtained for 3719 HI sources. However, 147 of these

⁴ The NASA/IPAC Extragalactic Database (NED) is operated by the Jet Propulsion Laboratory, California Institute of Technology, under contract with the National Aeronautics and Space Administration.

were found to be multi-galaxy systems and were thus excluded from our analysis.

2.2. WISE Photometry

WISE was launched in 2009 December, and mapped the entire sky in four mid-infrared bands: *W1*, *W2*, *W3*, and *W4* (3.4, 4.6, 12, and 22 μm ; Wright et al. 2010). Once *WISE* depleted its cryogen in 2010 October, it was then operated in a “warm” state using the two short bands and then placed in hibernation for well over 2 yr. As part of the *NEOWISE* program, *WISE* was reactivated in 2013 September and continues to observe in the *W1* and *W2* bands (Mainzer et al. 2014). The point source sensitivities of *W1*, *W2*, *W3*, and *W4* in Vega magnitudes are 16.5, 15.5, 11.2, and 7.9, respectively (Wright et al. 2010), in which *W4* is approximately two orders of magnitude more sensitive than the *IRAS*.

We have measured new *WISE* photometry for the optical counterparts of the HICAT source using the procedure described in Jarrett et al. (2013). We chose to do this because the profile-fit photometry data in the ALLWISE public-release archive (Cutri et al. 2013a) of the (degraded resolution) mosaics is optimized for point sources (e.g., Jarrett et al. 2013; Cluver et al. 2014, and references therein). Therefore, resolved sources such as our sample galaxies are either measured as several point sources, or their flux is underestimated by the PSF photometry (mpro). The *WISE* default catalogs do include extended source photometry for 2MASS Extended Source Catalog (2MXSC; Jarrett et al. 2000) galaxies, but the elliptical apertures (gmag) miss a significant fraction of the flux (Cluver et al. 2014).

All measurements are carried out on *WISE* image mosaics that are constructed from single native frames using a drizzle technique (Jarrett et al. 2012), resampled with 1 sq. arc pixels (relative to a 6 arcsec FWHM beam). Photometry for each individual HIPASS galaxy, principally flux measurements and surface brightness characterizations, are conducted using the system developed by T. H. Jarrett specifically for *WISE* data (Jarrett et al. 2013, see Section 3.6). The system estimates photometric errors from the formal components, including the sky background variance and the local sky level, instrumental signatures, and the absolute calibration. The error model also takes into account the correlation between resampled pixels through a correction factor, which is detailed in the *WISE* Explanatory Supplement (see Section 2.3.f, Cutri et al. 2013a). As detailed in Jarrett et al. (2013), the shape (inclination) and orientation were determined at a fixed 3σ isophotal level, which provides a robust and relatively accurate ($<5\%$) estimate, although this assumes symmetry and a fixed shape to the 1σ edge of the galaxy.

As detailed in T. H. Jarrett et al. (2013, 2018, in preparation), isophotal measurements at the *W1* 1σ level typically capture more than 96% of the total light for bulge-dominated galaxies, and to a lesser extent ($\geq 90\%$) for late-type galaxies, and most notably in the *W3* and *W4* bands as much as 20% of the light can be missing with low surface brightness galaxies. Hence, total fluxes are important in order to estimate the dust-obscured star formation activity in the *W3* and *W4* bands. The total flux is estimated by fitting a double Sérsic function to the axisymmetric radial profile, consisting of an inner bulge and an outer disk. Integrating the composite Sérsic model from the 1σ isophote to the edge of the galaxy (3 disk scale lengths) recovers the light that is below the single-pixel noise threshold;

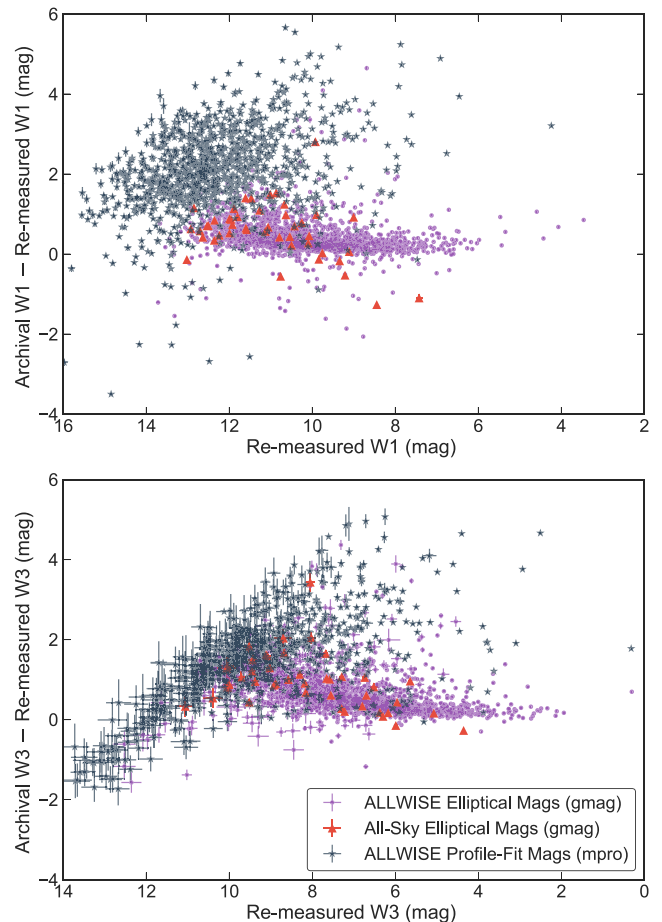


Figure 1. Difference between the archival and new magnitudes as a function of the new magnitude for *W1* (top) and *W3* (bottom). In order of preference, the archival data are either elliptical aperture magnitudes from the ALLWISE (purple) catalog or All-Sky magnitudes (navy) catalog, or PSF profile-fit (red) magnitudes from the ALLWISE catalog (Cutri et al. 2013b). For galaxies with $W1 \sim 12$ mag, the default elliptical aperture photometry is typically in error by ~ 1 mag, while the PSF profile-fit photometry is in error by ~ 2 mag.

details of the fitting process may be found in Jarrett et al. (2013). The error model for the total fluxes includes the goodness of fit, as well as the previous sky estimation per pixel estimates, and typically adds 4%–5% to the isophotal flux uncertainty.

Lastly, each galaxy mosaic is visually inspected, and if necessary, bright stars and nearby galaxies are manually masked out, and the apertures are adjusted. Figure 1 compares our new *WISE* photometry for HICAT galaxies with the previously available archival fluxes and illustrates the impact of the new photometry on derived quantities. For example, for $W1 \sim 12$ mag galaxies our *W1* and *W3* magnitudes are on average systematically brighter by ~ 1.4 mag and 1.1 mag than the default photometry pipeline magnitudes. Figure 2 shows four examples of the *WISE* mosaics that have been cleaned of neighboring objects, as well as the elliptical apertures used for photometry.

We apply an S/N threshold of 5 in the *W1* and *W2* bands, an S/N threshold of 3 in the *W3* band, and reject confused sources or H I sources consisting of multiple galaxies. Consequently, we measure good *W1*–*W2* photometry for 3275 H I sources and good *W1*–*W2*–*W3* photometry for 2831 H I sources. We find 20 H I sources that do not meet any of our *WISE* signal-to-noise

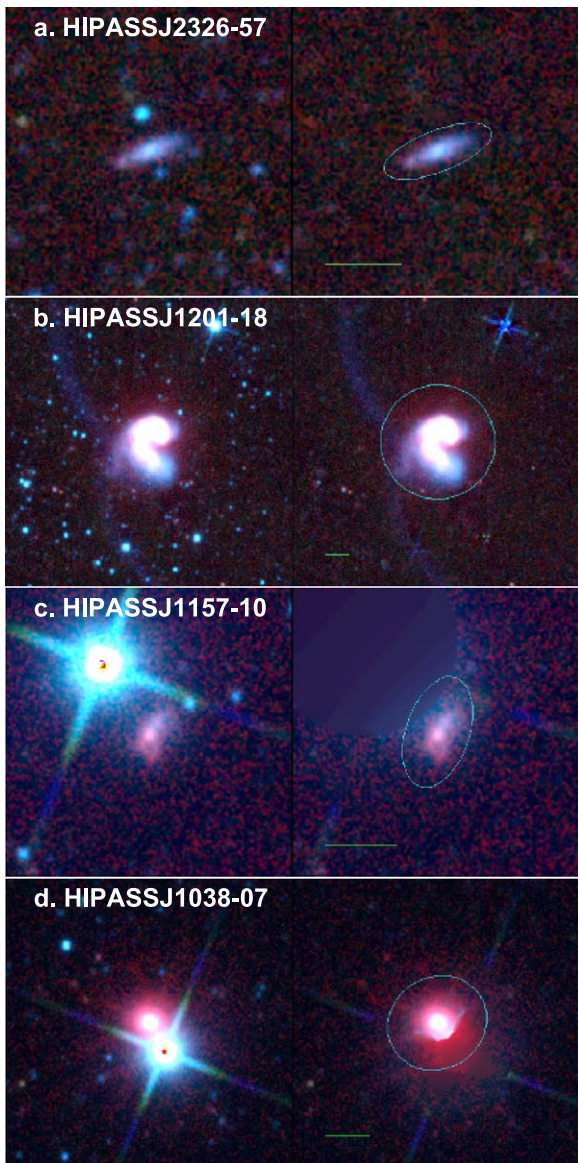


Figure 2. *WISE* color images composed of W1, W2, W3, W4 bands of four H I sources showing the galaxies before (left) and after (right) star and background source removal. The cyan ellipses indicate the 1σ apertures. The light from evolved stars is in blue and active star formation is in red. A scale of $2'$ is indicated by the green horizontal line. North is upwards and east is to the left. HIPASSJ2326-57 is an example of a well-behaved photometric galaxy; HIPASSJ1201-18 is a multi-galaxy H I source; HIPASSJ1157-10 and HIPASSJ1038-07 are both flagged visually and have a W1 and W2 S/N < 5 , respectively.

thresholds and 147 H I sources are multi-galaxy sources. From top to bottom, Figure 2 shows examples from HICAT of a “well-behaved” source, a multi-galaxy source, and two visually flagged sources. A full list of parameters for HICAT+*WISE* (H I-*WISE*) is given in Table 8 in the Appendix. The 147 H I sources that are found to be multi-galaxy systems are excluded from Table 8.

Figure 3 illustrates the *WISE* colors of HICAT galaxies, along with the expected colors of different types of galaxies, and clearly demonstrates that HIPASS is dominated by star-forming spiral galaxies, with relatively few ellipticals and luminous infrared galaxies (LIRGs). The galaxies with intermediate disk colors in the active galactic nucleus (AGN)/

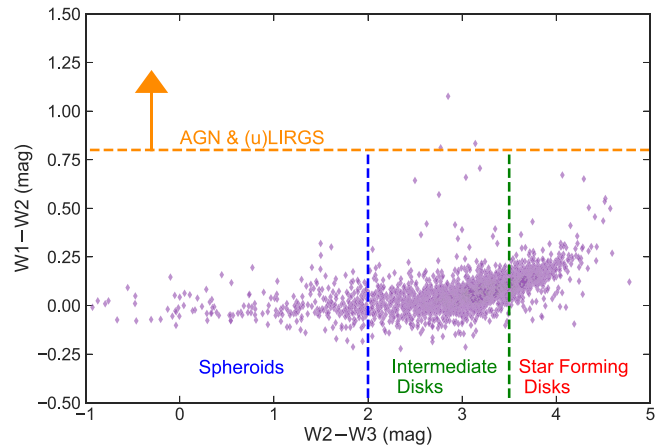


Figure 3. *WISE* mid-infrared colors of the HICAT sources with good *WISE* photometry. The horizontal and vertical lines denote the division between different types of galaxies (e.g., Jarrett et al. 2017). HICAT is dominated by star-forming, intermediate, or late-type disk galaxies.

LIRGs region may harbor dust-obscured AGNs and Seyferts (Jarrett et al. 2011; Huang et al. 2017).

3. Stellar Mass, H I Mass, and SFR Estimation

In this section, we will describe the methods used to estimate stellar mass, H I mass, and SFR for our samples. For these quantities, we compiled distances from (in order of preference) Cosmicflows-3 (Tully et al. 2016) and HICAT. When distances are not available in the Cosmicflows-3 database, we determine luminosity distances using HIPASS redshifts by applying a cosmic microwave background (CMB)-frame correction using the CMB dipole model presented by Fixsen et al. (1996), followed by an application of the LCDM. For samples selected by stellar mass (Sections 4.2 and 4.3), we include some galaxies that are not in HICAT, and for these galaxies, we use luminosity distances from velocities reported by NED in the same manner as stated above when distances are not available in the Cosmicflows-3 database. Table 8 lists these distances—and their respective sources—for each galaxy.

3.1. Stellar Mass

The W1 and W2 bands are dominated by light from K- and M-type giant stars, and thus trace the continuum emission from evolved stars with minimal extinction at low redshifts. Consequently, these bands are good tracers of the underlying stellar mass of a galaxy (Meidt et al. 2012; Cluver et al. 2014). However, the W2 band is also sensitive to hot dust, as well as $3.3 \mu\text{m}$ polycyclic aromatic hydrocarbon (PAH) emission from extreme star formation and AGNs. W1 contains the $3.3 \mu\text{m}$ PAH emission, but it is typically weak for normal star-forming galaxies (Ponomareva et al. 2018). As such, the aggregate stellar mass will be overestimated in the presence of an AGN (Jarrett et al. 2011; Stern et al. 2012; Meidt et al. 2014). In order to mitigate this problem, we exclude AGNs from our analysis that are identified in the AGN catalog of Véron-Cetty & Véron (2010).

Stellar masses were estimated following the GAMA-derived stellar mass-to-light ratio ($M_*/L_{W1\text{Sun}}$) relation of Cluver et al. (2014):

$$\log_{10} M_*/L_{W1\text{Sun}} = -1.96(W1 - W2) - 0.03, \quad (1)$$

which depends on the “in-band” luminosity relative to the Sun,

$$L_{W1_{\text{Sun}}} = 10^{-0.4(M - M_{\text{Sun}})}, \quad (2)$$

where M is the absolute $W1$ magnitude and $M_{\text{Sun}} = 3.24$ (Jarrett et al. 2013). Equation (1) was determined using the Galaxy and Mass (GAMA; Driver et al. 2009) survey with stellar masses derived assuming a Chabrier (2003) IMF (Taylor et al. 2011; Cluver et al. 2014), and limited to galaxies with $-0.05 < W1 - W2 < 0.30$, so we restrict the input colors for Equation (1) accordingly. The $W1 - W2$ color dependence takes into account morphological dependence on the M/L and other factors, such as metallicity (Cluver et al. 2014). To determine the $W1 - W2$ color, apertures are matched between the two bands. We typically use the $W2$ elliptical isophotal aperture as the fiducial since it is less sensitive than $W1$ and usually 10% to 15% smaller in radial extent. This is particularly the case for galaxies whose mid-infrared emission is dominated by stellar light (see Cluver et al. 2017; Jarrett et al. 2017).

The consistency of our stellar masses and those from other studies can be tested using the MPA-JHU catalog (Brinchmann et al. 2004)⁵ for the Sloan Digital Sky Survey (SDSS; York et al. 2000). By construction, our *WISE* stellar masses agree with the SED stellar masses determined by GAMA (Driver et al. 2009; Taylor et al. 2011), with a 1σ scatter of just 0.2 dex, and the GAMA M_*/L agree with the MPA-JHU M_*/L , with a bi-weight mean and 1σ scatter in the difference between M_*/L of -0.01 and 0.07 dex. For dwarf galaxies the difference MPA-JHU between and UV-optical SED stellar masses (Huang et al. 2012) is zero with the objects lying within ± 0.35 dex M_{\odot} (Maddox et al. 2015, and private correspondence). Thus, we do not expect large offsets between the stellar masses we have obtained from *WISE* and those which have been used in recent studies of H I galaxies.

3.2. H I Mass

To calculate the H I mass, we use the published integrated 21 cm flux ($F_{\text{H I}}$) as follows:

$$M_{\text{H I}}[M_{\odot}] = \frac{2.356 \times 10^5}{1+z} \times D_L^2 \times F_{\text{H I}}[\text{Jy km s}^{-1}], \quad (3)$$

where D_L is the luminosity distance to the galaxy in megaparsecs and z is the redshift measured from the H I spectrum (e.g., Lutz et al. 2017). The uncertainty in the H I mass ($\Delta M_{\text{H I}}$) is estimated using the method suggested by Doyle & Drinkwater (2006):

$$\Delta F_{\text{H I}} = 0.5 \times F_{\text{H I}}^{1/2}, \quad (4)$$

$$\Delta M_{\text{H I}} = M_{\text{H I}} \frac{\Delta F_{\text{H I}}}{F_{\text{H I}}}. \quad (5)$$

3.3. Star Formation Rate

The $W3$ and $W4$ bands are sensitive to the interstellar medium, AGNs, and star formation (e.g., Calzetti et al. 2007; Jarrett et al. 2011; Cluver et al. 2014, 2017). $W4$ emission is dominated by warm dust, and for star-forming galaxies $W4$ luminosity can be used to predict Balmer-decrement-corrected $\text{H}\alpha$ luminosity with an accuracy of 0.2 dex (Brown et al. 2017).

However, $W4$ lacks sensitivity and 39% of HICAT sources lack $W4$ detections.

WISE $W3$ luminosity includes contributions from PAHs, nebular emission lines, silicate absorption, and warm dust, all of which are associated with star formation in galaxies. For $\sim L^*$ star-forming galaxies, Cluver et al. (2017) found that PAHs and warm dust make 34% and 62.5% contributions, respectively, to the observed $W3$ luminosity. That said, we expect the contribution of PAHs to the $W3$ luminosity to decrease with decreasing galaxy mass due to the mass–metallicity relation of galaxies. Also, $W3$ better predicts the total infrared luminosity (and hence SFR) than $W4$ (Cluver et al. 2017). *WISE* $W3$ is thus a good SFR indicator, and can be used to obtain the Balmer-decrement-corrected $\text{H}\alpha$ luminosity with an accuracy of 0.28 dex (i.e., Brown et al. 2017).

Although the $W3$ band traces emission from star formation, it may also have contributions from evolved stellar populations. For $\sim L^*$ galaxies located at the center of the star-forming main sequence, the stellar continuum contributes 15.8% of the $W3$ light and we subtract it from our data using the $W1$ photometry and the method of Helou et al. (2004). To account for this, we therefore scale the $W1$ integrated flux density, and subtract it from the $W3$ total flux to give an estimate of the $W3$ emission from the ISM, $W3_{\text{PAH}}$ (Cluver et al. 2017). We use the prescription in Table 4 from Brown et al. (2017) to estimate the Balmer-decrement-corrected $\text{H}\alpha$ ($L_{\text{H}\alpha, \text{Corr}}$):

$$\log L_{W3_{\text{PAH}}} [\text{erg s}^{-1}] = (40.79 \pm 0.06) + (1.27 \pm 0.04) \times (\log L_{\text{H}\alpha, \text{Corr}} [\text{erg s}^{-1}] - 40), \quad (6)$$

with a 1σ scatter of 0.28 dex. SFRs are estimated by scaling the Kennicutt (1998) calibration to a Chabrier (2003) IMF:

$$\text{SFR} [M_{\odot} \text{ yr}^{-1}] = (4.6 \times 10^{-42}) \times L_{\text{H}\alpha, \text{Corr}} [\text{erg s}^{-1}]. \quad (7)$$

The uncertainty in SFR is dominated by the scatter in the relationship between *WISE* $W3$ luminosity and Balmer-decrement-corrected $\text{H}\alpha$ luminosity and therefore the uncertainty in $\log(\text{SFR}) \sim 0.28$ dex (Brown et al. 2017).

We use the SFR calibration from Brown et al. (2017) because it provides better SFR estimates for a broad range of galaxies—including LIRGs and blue compact dwarfs galaxies—compared to the prior literature. Also, Cluver et al. (2017) compared the SFR calibrations from the prior literature to their calibration derived from total infrared luminosity and found the SFR calibration from Brown et al. (2017) to agree with their own.

4. Samples

We create three samples to address specific science questions: an H I-selected sample (H I sample), a stellar mass-selected sample (M_* sample), and a spiral sample. In addition to addressing specific science questions, these samples allow us to compare to the prior literature and to explore the impact that galaxy morphology and selection bias have on the scaling relationships between star formation, stellar mass, and H I mass.

For the remainder of the paper we focus on galaxies (including 3513 HICAT galaxies) that are at least 10° away from the Galactic plane and are not known AGNs (from the Véron-Cetty & Véron (2010) catalog), although we do include some additional galaxies in our summary of galaxy coordinates, redshifts, and photometry provided in Table 8. We also

⁵ Available via <http://www.mpa-garching.mpg.de/SDSS/>.

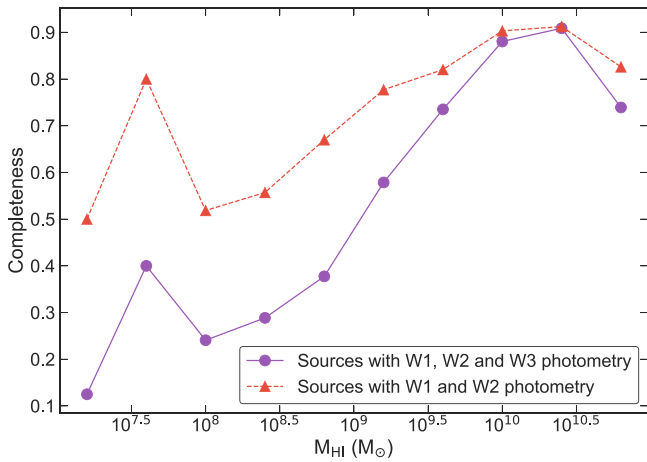


Figure 4. Fraction of HICAT sources with *WISE* photometry, compared to the total sample, as a function of H I mass. Out of 3513 HICAT sources, 80% have good W1 and W2 detections and 68% have good W3 detections.

exclude objects north of the main HICAT footprint ($\delta \geq +2$) from the M_s sample and spiral sample.

4.1. H I-selected Sample

We use HICAT to form the basis of the H I-selected sample. Out of 3513 HICAT sources, 2826 have good W1 and W2 photometry. Of these, 2396 also have good photometry for the W3 band, and 2342 galaxies in this category have significant $W3_{\text{PAH}}$ flux (W3 flux with the stellar continuum subtracted). Figure 4 shows the percentage of H I sources with *WISE* counterparts as a function of H I mass. We achieve a HICAT-*WISE* match completeness of 80% for H I mass $>10^{9.5} M_{\odot}$.

4.2. Spiral Sample

To measure the distribution of H I masses and SFRs as a function of stellar mass and morphology, we generate a stellar mass-selected sample of spiral galaxies (the spiral sample). The spiral sample is drawn from the Bonne et al. (2015) catalog, which achieves a 99% completeness in redshifts and morphologies for galaxies with $K_{\text{tot}} < 10.75$. We maximize H I completeness by limiting the sample to spiral galaxies (defined with de Vaucouleurs T-type ≥ 0) with redshift ≤ 0.01 and remeasured W1 magnitude < 10 . Our spiral sample consists of 600 galaxies.

For 435 of our spiral galaxies we obtained H I fluxes from HICAT, while for a further 121 galaxies we obtained archival H I fluxes from Paturel et al. (2003), Huchtmeier & Richter (1989), Springob et al. (2005), and Masters et al. (2014). The details of the H I counterparts are provided in Table 2. As we illustrate in Figure 5, 93% of the spiral galaxies have H I detections.

The aforementioned W1 and redshift limits are chosen because of the brightness limitation of the parent sample and the detection sensitivity of HICAT. While the notional limit for the Bonne et al. (2015) is $K_{\text{tot}} \leq 10.75$, this limits the $W1 \leq 11.5$ and galaxy numbers decline at $W1 > 10$. Table 3 lists the number of galaxies in our sample, the number with H I detections and the percentage with H I detections with and without the redshift and W1 magnitude limits applied. Removing the redshift and magnitude limits from the spiral sample decreases the percentage of galaxies with H I detections to 50%, but has little impact on measured relations we describe in Section 5.

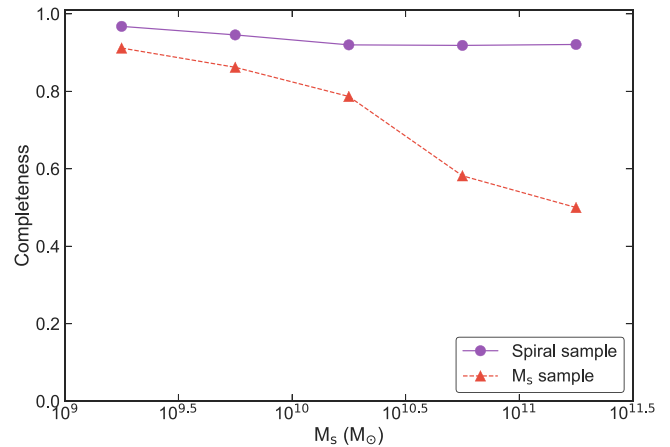


Figure 5. Fraction of galaxies in the spiral sample and the M_s sample with H I mass measurements. For the spiral sample, 556 out of 600 galaxies have a H I counterpart, giving the spiral sample a completeness of 93%. 590 galaxies out of the 839 galaxies in the M_s sample have a H I counterpart.

Table 2
The Number of Galaxies the Spiral Sample and the M_s Sample with H I Counterparts

H I Source	Spiral Sample	M_s Sample
Total	600	839
HICAT	435	454
Paturel et al. (2003)	100	114
Huchtmeier & Richter (1989)	13	13
Springob et al. (2005)	1	2
Masters et al. (2014)	7	7

4.3. Stellar Mass-selected Sample (M_s Sample)

In order to compare the H I mass, stellar mass, and SFR relationships of this work to those of GASS (Catinella et al. 2010, 2012, 2013), which uses a stellar mass-selected sample, we have also produced such a sample (M_s sample). The GASS sample is designed to measure the neutral hydrogen content of 1000 galaxies to investigate the physical mechanisms that regulate how cold gas responds to different physical conditions in the galaxy and the processes responsible for the transition between star-forming spirals and passive ellipticals (Catinella et al. 2010).

The M_s sample selection is identical to that of the spiral sample except that it lacks the T-type criterion. The M_s sample contains 839 galaxies, of which 590 have an H I counterpart. The details of the H I counterparts are provided in Table 2. Figure 5 shows that the fraction of galaxies with an H I measurement drops at the higher stellar masses, where the number of H I-poor ellipticals increases.

5. $M_{\text{HI}}-M_*$ Relationship

In this section, we will look at the relationship between H I mass and stellar mass for all three samples. The H I–stellar mass relation is one of the principal means used to provide insight to the history of gas accretion and star formation. Also, as discussed in Section 7, it can be used to test models of the stability of H I disks and how these disks can fuel star formation (Obreschkow et al. 2016; Wong et al. 2016). For each sample, we bin the data into stellar mass bins with a width of $\log(M_*) = 0.5$ and for bins with ≥ 10 galaxies we measure the median H I mass and 1σ scatter in H I mass for each stellar

Table 3
The Basic Properties of Our Spiral Sample and Spiral Galaxy Samples without the Redshift and W1 Selection Criteria Applied

	Spiral Sample	No W1-mag cut	No Redshift Cut	No W1 Magnitude and Redshift Cuts Applied
Total # of galaxies	600	792	1442	3458
# H I counterparts	556	672	1048	1697
% with H I counterpart	93%	87%	73%	50%

Table 4
Median H I Mass and 1σ (68%) Scatter as a Function of Stellar Mass for the Spiral Sample, and the GASS Spiral Sample

$\log(M_*)$ (M_\odot)	Spiral Sample				GASS Spiral Sample			
	$\log(M_{\text{HI}})$ (M_\odot)	1σ (M_\odot)	Total	% H I Detections	$\log(M_{\text{HI}})$ (M_\odot)	1σ (M_\odot)	Total	% H I Detections
9.25	9.14	0.42	31	97				
9.75	9.41	0.37	129	95				
10.25	9.59	0.43	225	92	9.53	0.47	130	89
10.75	9.61	0.46	174	97	9.73	0.38	111	94
11.25	9.93	0.54	38	92	9.88	0.55	64	83

Note. Median H I masses are not calculated for stellar mass bins with a H I completeness $\leq 50\%$.

mass bin. The 1σ scatter about the median is determined using the range encompassing 68% of the data. For the spiral sample and M_s sample, care is needed when accounting for the galaxies with H I nondetections. When estimating the median H I mass as a function of the stellar mass, we assume the H I upper limits are below the median H I mass for the relevant stellar mass bin, which is a reasonable approximation when the H I detection rate is $\gg 50\%$. The median H I masses are determined for any stellar mass bin with 10 or more galaxies and H I detection rate above 50%. Upper limits for individual galaxies are determined using the integrated flux of 7.5 Jy km s^{-1} , corresponding to the HICAT's 95% completeness limit (Zwaan et al. 2004).

While we list the individual uncertainties in Table 8, we find that W1 ~ 12 galaxies have a stellar mass uncertainty ≤ 0.2 dex, and this uncertainty decreases with increasing W1 flux. Also, 80% of the H I sample has an H I mass uncertainty better than 20%.

5.1. H I Sample

The relationship between H I mass and stellar mass for the H I-selected sample is illustrated in Figure 6. The H I mass is a strong function of stellar mass among the H I sample (Spearman's rank correlation, $r_s = 0.64$) and the least-squares fit to the medians, represented by an orange line in Figure 6, is

$$\log M_{\text{HI}} = 0.51 (\log M_* - 10) + 9.71. \quad (8)$$

We fit 68% of the H I masses within 0.5 dex of our best-fit relation.

H I mass versus stellar mass relations for the H I-selected sample and previous studies (Catinella et al. 2010; Huang et al. 2012; Maddox et al. 2015) are also plotted in Figure 6. Our sample and the ALFALFA samples of Huang et al. (2012) and (Maddox et al. 2015) are H I-selected, while the GASS sample of Catinella et al. (2010) is stellar mass-selected. We find the relations for the H I-selected samples are qualitatively similar, with median H I mass increasing with stellar mass. In contrast, the H I versus stellar mass relation measured with the GASS sample (Catinella et al. 2010) is up to 0.5 dex lower than those derived from H I-selected samples, as the GASS sample includes galaxies with low H I

masses (including ellipticals). There are also discrepancies in the H I versus stellar mass relations measured with different H I-selected samples. We do not see the break in the relation at a stellar mass of $10^9 M_\odot$ that was previously observed by ALFALFA (i.e., Huang et al. 2012; Maddox et al. 2015).⁶ Below a mass of $10^9 M_\odot$ our sample is less than 70% complete for WISE counterparts, and thus we may not be reliably measuring H I mass versus stellar mass in this mass range. However, even if this was not an issue we believe this sample would produce a biased relation, as it (by construction) excludes galaxies that have high stellar masses but low H I masses (i.e., many elliptical galaxies).

5.2. Spiral Sample

The H I and stellar mass distribution for the spiral sample is shown in Figure 7. The median H I mass increases with stellar mass with a least-squared fit of

$$\log M_{\text{HI}} = 0.35 (\log M_* - 10) + 9.45, \quad (9)$$

with 68% of the H I masses within 0.4 dex.

However, as Figure 7 illustrates, at a given stellar mass the median H I mass increases with T-type while the dispersion decreases with T-type. For example, for the 10^{10} to $10^{10.5} M_\odot$ stellar mass bin, the median H I mass and the 1σ spread of galaxies for all spirals is $10^{9.53} M_\odot \pm 0.47$ dex, for T-type 0 to 2 is $10^{9.26} M_\odot \pm 0.59$ dex, and for T-type 6 to 8 is $10^{9.72} M_\odot \pm 0.31$ dex. The increasing spread of H I masses with decreasing T-type for spiral galaxies may be part of a broader trend, as Serra et al. (2012) concluded that the H I mass distribution for early-type galaxies was far broader than that for spirals. They suggest this scatter reflects the large variety of H I content of early-type galaxies, and confirms the lack of correlation between H I mass and luminosity.

In Figure 7, we compare our H I mass–stellar mass distribution of our spiral sample to that from GASS (Catinella

⁶ The slopes of the least-squared fits for Figure 6 is 0.65 ± 0.014 for stellar masses $\leq 10^9 M_\odot$ and 0.48 ± 0.013 for stellar mass $> 10^9 M_\odot$ and therefore are consistent with each other. Meanwhile, Huang et al. (2012) measured a slope of 0.712 for stellar masses $\leq 10^9 M_\odot$ and 0.276 for stellar masses $> 10^9 M_\odot$.

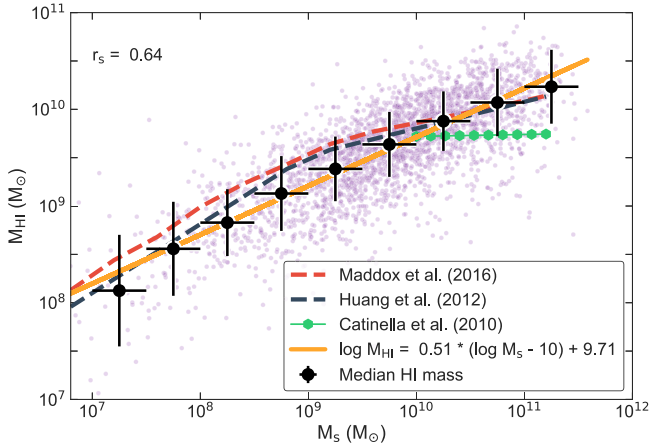


Figure 6. H I mass vs. stellar mass of the H I-selected sample. Spearman's rank correlation, r_s , is listed in the top left corner. Our median H I masses are slightly below those derived by Huang et al. (2012; blue dashed line), and Maddox et al. (2015; red dashed line), who both used ALFALFA H I-selected samples. However the H I mass medians of the H I sample are higher than the GASS sample (green solid-line; Catinella et al. 2010), which is a stellar mass-selected sample. H I samples overestimate H I mass as a function of stellar mass because H I samples do not detect galaxies with low H I mass, such as ellipticals.

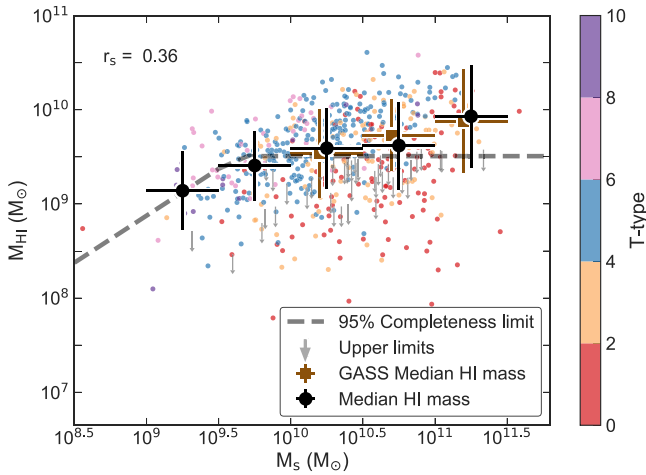


Figure 7. H I mass vs. stellar mass for the (highly complete) spiral sample. Symbols are color-coded by morphology, the median H I masses are shown for the spiral sample (black circles) and the GASS sample (brown squares; Catinella et al. 2010). The dashed line shows the H I mass limit for $z \leq 0.01$ and $W1 \leq 10$ star-forming galaxies. The Spearman's rank correlation coefficient is shown in the top left. H I mass is a function of both T-type and stellar mass. The median H I masses increases with stellar mass with a power-law index of 0.35.

et al. 2010), using GASS galaxies that we have classified as spirals with Galaxy Zoo 1 (GZ1; Lintott et al. 2011). Using the GZ1 classifications and a 70% vote threshold, we find GASS comprises 305 spirals, 273 ellipticals, and 182 galaxies with uncertain morphology.⁷ We repeat our analysis on the GASS sample, using the same stellar mass bins and H I median mass calculations with stellar mass bins with 10 or more galaxies and an H I detection rate $>50\%$. The estimated median H I masses

⁷ Using the default criteria of 80% vote threshold (see the following references for details on Galaxy Zoo and the data release: Lintott et al. 2008, 2011), 291 galaxies (39%) in GASS are classified as unknowns. We have decreased the vote requirement to 70% to decrease the number of unknowns to 182 galaxies (24%), although we find this has little impact on our measured relations.

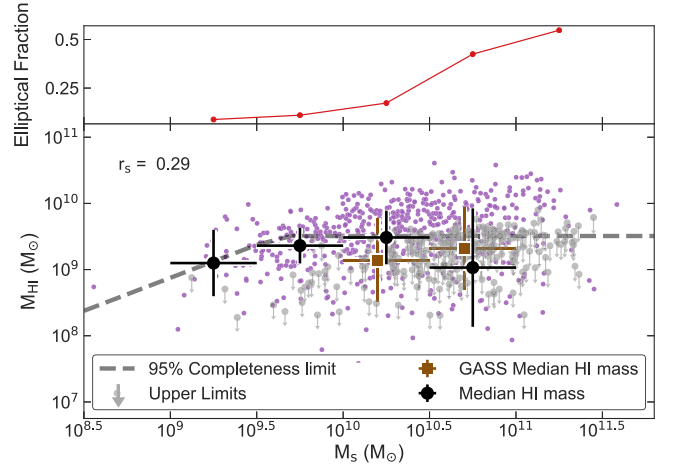


Figure 8. Spiral fraction vs. stellar mass (upper panel) and H I mass vs. stellar mass (lower panel) for the M_* sample. Median H I masses are shown for the M_* sample (black circles) and the GASS sample (brown squares; Catinella et al. 2010). The HIPASS mass limit for galaxies at $z \leq 0.01$ and $W1 \leq 10$ is shown by the gray dashed line and the Spearman's rank correlation coefficient is shown in the top left. H I mass is almost flat with increasing stellar mass for both samples, in large part because of the increasing fraction of passive early-type galaxies with increasing stellar mass.

for the spiral sample and the GASS spiral samples are listed in Table 4. The median H I masses for the GASS spiral sample increases with stellar mass similar to our spiral sample. The median H I mass of the spiral samples differs by about 0.08 dex on average. To explain the relationship between H I mass and stellar mass of the spiral samples we turn to the halo spin parameter models of Obreschkow et al. (2016) in Section 7.

5.3. M_* Sample

In Figure 8, we present H I mass versus stellar mass for our M_* sample and the equivalent stellar mass-selected sample of GASS (Catinella et al. 2010). The estimated median H I masses of the M_* sample and the GASS sample are listed in Table 5. For the M_* sample the H I mass increases with the stellar mass for the stellar mass bins $\leq 10^{10.5} M_*$ and then flattens for the highest stellar mass bin. The estimated H I mass median for the highest stellar mass bin may be underestimated, as the H I completeness for this bin is only 58% and our assumption that all nondetections are below the median could be in error.

At stellar masses greater than $10^{10} M_\odot$, median H I mass is almost constant with stellar mass, and our measurements agree with those of GASS to within 0.3 dex. This is in contrast with the trend shown in Figure 7 for the spiral sample. The obvious explanation, given the prior literature (e.g., Catinella et al. 2010; Huang et al. 2012), is that this is due to the increasing fraction of gas poor early-type galaxies at high M_* , as illustrated in the top panel of Figure 8. Serra et al. (2012) found that early-type galaxies host less H I than spiral galaxies, but have a broader range of H I masses. For example, Serra et al. (2012) found that elliptical galaxies have H I mass from 10^7 to $10^9 M_\odot$ (the lower limit is uncertain as this overlooks H I nondetections in their sample), while the H I mass distribution for spirals peaks at $\sim 2 \times 10^9 M_\odot$, with a small number of galaxies below $10^8 M_\odot$. Combining this result with our previous findings from our spiral sample, we conclude that as one moves from early-type to late-type galaxies, median H I mass increases while the scatter in H I mass decreases. Within an individual T-type, H I mass typically increases with stellar

Table 5
Median HI Mass and 1σ (68%) Scatter as a Function of Stellar Mass for the M_s Sample and the GASS Sample

$\log(M_*)$ (M_\odot)	M_s Sample				GASS Spiral Sample			
	$\log(M_{\text{HI}})$ (M_\odot)	1σ (M_\odot)	Total	% HI Detections	$\log(M_{\text{HI}})$ (M_\odot)	1σ (M_\odot)	Total	% HI Detections
9.25	9.10	0.50	34	91				
9.75	9.56	0.27	145	86				
10.25	9.48	0.41	272	79	9.14	0.64	299	68
10.75	9.03	0.89	299	58	9.32	0.62	292	63
11.25			84	50			168	50

Note. Median HI masses are not calculated for stellar mass bins with an HI completeness $\leq 50\%$.

mass, and it is the increasing fraction of early-types with increasing stellar mass that explains the roughly constant median HI masses measured for the M_s sample.

5.4. The Impact of Sample Selection

A key conclusion from the previous sections is that sample selection impacts measured HI mass versus stellar mass relations, and, to illustrate this, in Figure 9 we plot HI mass–stellar mass relations for HI-selected samples, spiral galaxy samples, and stellar mass-selected samples, including data from both our work and the literature. For all values of stellar mass, HI-selected samples have a higher HI mass than spiral-selected and stellar mass-selected samples. This is because HI surveys are designed to sample a large number of HI-rich systems, and therefore lack the sensitivity to detect the HI-poor galaxy population. For example, HIPASS can detect galaxies with HI masses $>10^9 M_\odot$ at $z = 0.01$; however, elliptical galaxies have HI masses $\leq 10^9 M_\odot$ (Serra et al. 2012), and would thus be largely missing from HIPASS samples at these redshifts. Even the late-type galaxies in Figure 7 have HI masses as low as $10^8 M_\odot$, and thus some are missing from HIPASS-selected samples at $z > 0.01$. Similar selection effects apply to ALFALFA, albeit at higher redshifts. This is not surprising and indeed was a motivation for studies such as GASS, but does illustrate that HI mass versus stellar mass relations have a strong dependence on sample selection.

6. Star-forming Properties of the Spiral Sample

6.1. Star-forming Main Sequence

While the relationship between SFR and HI mass is the principal focus of the paper, we are also able to measure the local ($z \leq 0.01$) star-forming main sequence (MS; e.g., Noeske et al. 2007; Rodighiero et al. 2011; Wuyts et al. 2011) using the spiral sample. Measurements of the MS are enhanced by our highly complete sample, our new *WISE* photometry (which should mitigate aperture bias—see Section 2.2), and our ability to take advantage of a recent calibration of *W3* as an SFR indicator that uses large aperture photometry (Brown et al. 2017).

In Figure 10 we present our star-forming main sequence. As expected, the median of the log SFR increases from -0.50 dex for the 10^9 to $10^{9.5} M_\odot$ stellar mass bin to 0.14 dex for the 10^{10} to $10^{10.5} M_\odot$ stellar mass bin, with the scatter of individual galaxies about the median being ~ 0.3 dex. For stellar mass bins above $10^{10} M_\odot$, the median log SFR is roughly constant at 0.14 while the scatter of the individual galaxy SFRs about the median increases from 0.38 to 0.49 dex. The changing trend of SFR with increasing stellar mass and the increased dispersion of

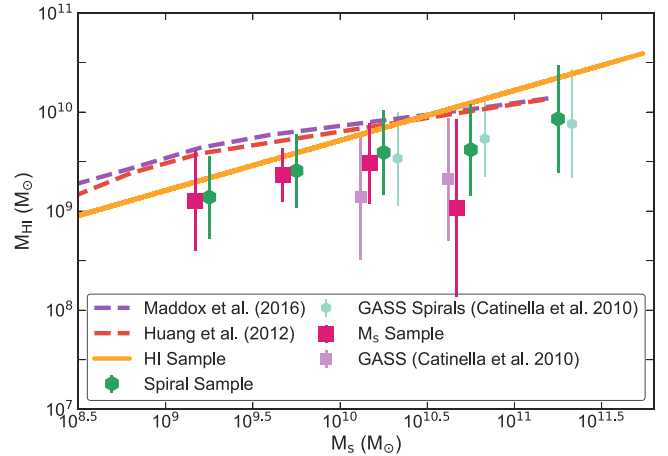


Figure 9. Comparison of HI mass vs. stellar mass for our HI-selected sample, the spiral sample, the M_s sample (without morphological criteria), and the prior literature. HI-selected samples give consistently higher relations than the other samples, as (by definition) they exclude galaxies with comparatively low HI masses.

SFRs is evidence of mass quenching (Kauffmann et al. 2003), and this also coincides with an increasing fraction of early-type spirals (T-type ≤ 2). To mitigate the effect of mass quenching on our model fit to the MS, we only fit to galaxies with stellar mass $\leq 10^{10.5} M_\odot$ (shown in Figure 10(b)) and measure the MS to be

$$\log \text{SFR} = 0.7 (\log M_* - 10) - 0.09, \quad (10)$$

with a 1σ scatter of 0.27 dex. Alternate selection criteria to mitigate the effect of mass quenching produces similar MS fits. For example, a subsample of galaxies with T-type > 2 produces a fit of $\log \text{SFR} = 0.61 (\log M_* - 10) - 0.08$ (1σ scatter = 0.26 dex).

Figure 10(b) and Table 6 also compare the MS relation from this work to the prior literature (Elbaz et al. 2007; Salim et al. 2007; Chen et al. 2009; Oliver et al. 2010; Zahid et al. 2012; Grootes et al. 2013), with data taken from the extensive review by Speagle et al. (2014). To shift the Speagle et al. (2014) homogenized MS relations from a Kroupa to Chabrier IMF, we apply -0.03 and -0.07 dex shifts to the stellar masses and SFRs, respectively. The blue line is the $z = 0.01$ MS relation given by Equation (28) from Speagle et al. (2014), and the shaded region is the “true” scatter about the MS (for more details, please refer to Speagle et al. 2014). The normalization (at $\log M_* = 10$) of our best fit is 0.04 dex smaller and the slope is 0.21 larger than the best fit for the MS of Speagle et al. (2014). Speagle et al. (2014) noted that the wide range of the

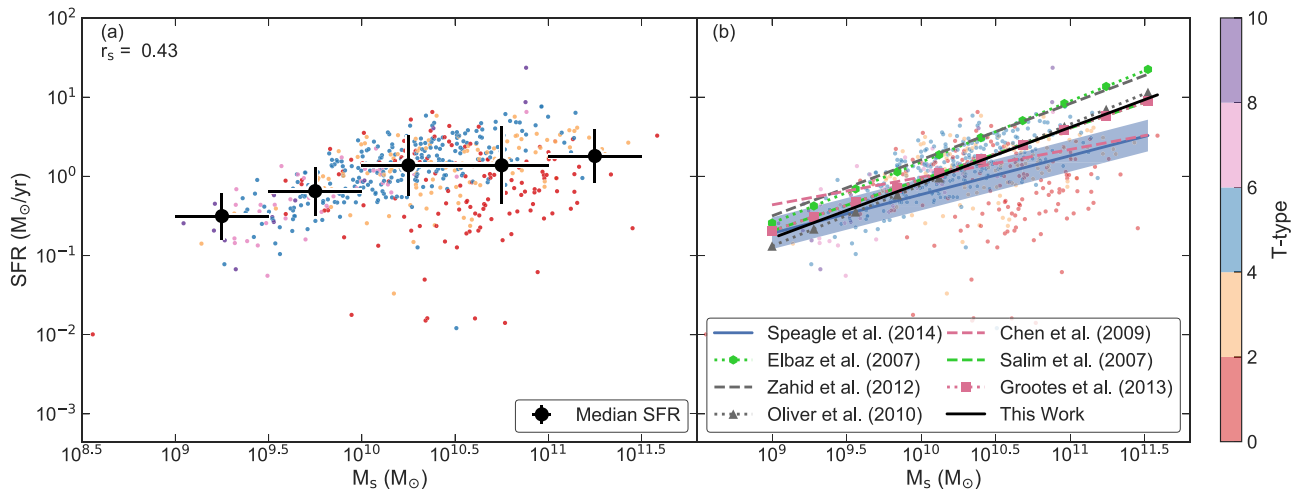


Figure 10. SFR vs. stellar mass for the spiral sample with symbols color-coded by morphology. The median SFRs are also shown in panel (a). The median SFR increases with stellar mass for $M_* < 10^{10.5} M_\odot$ and then flattens for $M_* > 10^{10.5} M_\odot$, indicating evidence of mass quenching. To mitigate the effect of mass quenching, we model the MS using spiral galaxies with $M_* < 10^{10.5} M_\odot$ and find $\log \text{SFR} = 0.7 \times (\log M_* - 10) - 0.09$. As illustrated by panel (b), $z \sim 0.01$ relations compiled by Speagle et al. (2014) show considerable scatter, and this may result (in part) from how studies exclude (or include) high-mass spirals that may have already commenced quenching.

MS slopes for the local universe suggests that the systematics involved are underestimated, and they estimate the magnitude of these systematics on the MS slopes to be of the order of ~ 0.2 dex. As we noted earlier, our slope depends on the criterion used to reject galaxies that could be undergoing quenching, and including early-type spiral galaxies with masses above $10^{10.5} M_\odot$ reduces our slope to 0.416 (1σ scatter = 0.34), which is closer to that of Speagle et al. (2014).

6.2. Star Formation Efficiency

SFE, defined as SFR/M_{HI} , quantifies the current rate of gas consumption, dividing the SFR by HI mass and SFE is expected to depend on the stellar mass of a galaxy (Schiminovich et al. 2010; Huang et al. 2012; Wong et al. 2016; Lutz et al. 2017). SFE and its inverse, the depletion time, have thus been commonly used to quantify gas consumption and test models of the stability of galactic disks (e.g., Wong et al. 2016).

To investigate the relationship between star formation and HI mass within the spiral sample, we plot in Figure 11 SFE as a function of stellar mass. In Table 7 we provide the median SFEs as a function of stellar mass, with the upper limits on the HI mass being used for the HI nondetections. The SFE remains relatively constant at a median SFE = $10^{-9.57} \text{ yr}^{-1}$, with a 1σ scatter of 0.44 dex for spiral galaxies with stellar masses between $10^{9.0}$ and $10^{11.5} M_\odot$. While we see evidence for mass quenching in high stellar mass spirals in Figure 10, the SFE appears to be constant for spiral galaxies falling on the MS and spiral galaxies that have (potentially) commenced quenching.

SFE versus stellar mass relations for both the spiral sample and previous studies (Schiminovich et al. 2010; Jaskot et al. 2015; Wong et al. 2016; Lutz et al. 2017) are compared in Figure 12(a). HI-selected samples (Jaskot et al. 2015; Lutz et al. 2017) exhibit an increasing SFE with stellar mass; however, this reflects their selection bias against galaxies with low HI masses. By contrast, stellar mass-selected samples (Schiminovich et al. 2010; Wong et al. 2016) exhibit a constant SFE with stellar mass; however, previous studies have

measured differing values of this constant, ranging from $10^{-9.65} \text{ yr}^{-1}$ (Wong et al. 2016) to $10^{-9.5} \text{ yr}^{-1}$ (Schiminovich et al. 2010). Wong et al. (2016) provide two theoretically motivated relations for SFE versus stellar mass, which are both plotted in Figure 12(b). The first relation assumes that the molecular gas fraction depends only on the stellar surface mass density, while the second assumes that this fraction depends on the hydrostatic pressure. Between stellar masses of $10^{9.0}$ and $10^{11.5} M_\odot$, the hydrostatic pressure model of Wong et al. (2016; which gives a constant SFE) shows the greatest consistency with our work and other stellar mass-selected samples.

7. Discussion

7.1. Is there an Upper Limit to the M_{HI} ?

For the spiral sample, we find that HI mass increases with stellar mass, from $10^{9.14} M_\odot$ at a stellar mass of $10^{9.25} M_\odot$ to $10^{9.93} M_\odot$ at a stellar mass of $10^{11.25} M_\odot$ (see Figure 7). We also observe a stellar mass-dependent upper limit on HI mass. In this section, we discuss the reason for this upper limit.

Both our HI- and stellar mass-selected samples imply an upper limit for HI mass as a function of stellar mass, and such thresholds are also seen in prior literature (e.g., Maddox et al. 2015). Is this upper limit for HI mass expected from theory? Maddox et al. (2015) argue that the maximum HI fraction for galaxies with stellar masses $> 10^9 M_\odot$ is set by the upper limit in the halo spin parameter, λ . The halo spin parameter is defined as

$$\lambda \equiv J_{\text{halo}} E_{\text{halo}}^{1/2} G^{-1} M_{\text{halo}}^{-5/2}, \quad (11)$$

where J_{halo} is the galaxy halo's angular momentum, E_{halo} its total energy, and M_{halo} its total mass (Boissier & Prantzos 2000). Maddox et al. (2015) determined the halo spin parameter of the ALFALFA galaxies and found that, at a fixed stellar mass, galaxies with the largest HI mass also have the largest halo spin parameter (see their Figure 6). The large halo spin of a galaxy stabilizes the high HI mass disk, preventing it from collapsing and forming stars.

Table 6
 Main-sequence Relationships

Paper	α	β	$\log \text{SFR}(10)$	z_{med}	z_{range}	$\log M_*$ Range	Survey
This Study	0.7	-7.09	-0.09	...	≤ 0.01	9.0–11.0	WISE
Zahid et al. (2012)	0.71 ± 0.01	-6.78 ± 0.1	0.32	0.07	0.04–0.1	8.5–10.4	SDSS
Oliver et al. (2010)	0.77 ± 0.02	-7.88 ± 0.22	-0.18	0.1	0.0–0.2	9.1–11.6	SWIRE
Chen et al. (2009)	0.35 ± 0.09	-3.56 ± 0.87	-0.06	0.11	0.005–0.22	9.0–12.0	SDSS
Elbaz et al. (2007)	0.77	-7.44	0.26	0.06	0.015–0.1	9.1–11.2	SDSS
Salim et al. (2007)	0.65	-6.33	0.17	0.11	0.005–0.22	9.0–11.1	GALEX-SDSS selected
Speagle et al. (2014)	0.49	-5.13	-0.03
Grootes et al. (2013) ^a	0.550	-5.520	-0.02	...	≤ 0.13	9.5–11	GAMA/Herschel-ALTAS
Cluver et al. (2017) ^b	1.05 ± 0.09	-10.40 ± 0.88	0.09	...	$z < 0.01 (< 30 \text{ Mpc})$	7–11.5	SINGS/KINGFISH

Notes. Column 1: reference. Columns 2 and 3: MS slope α and normalization β reported in Table 6 of Speagle et al. (2014). These best-fit parameters have been adjusted for IMF, cosmology, SPS model, and emission line corrections. Column 4: log SFR predicted by each MS relation at $\log M_* = 10$. Column 5: the median redshift. Column 6: redshift range. Column 7: stellar mass range. Column 8: survey data.

^a The normalization was not adjusted by Speagle et al. (2014). We do not apply shifts to the stellar masses and SFRs as Grootes et al. (2013) make use of Chabrier (2003) IMF.

^b The normalization was not adjusted for systematics by Speagle et al. (2014). The MS trend of Cluver et al. (2017) is not shown in Figure 10 because KINGFISH galaxies were chosen to cover the full range of galaxy types, luminosities and mass properties, and local ISM environments rather than being a magnitude-limited sample.

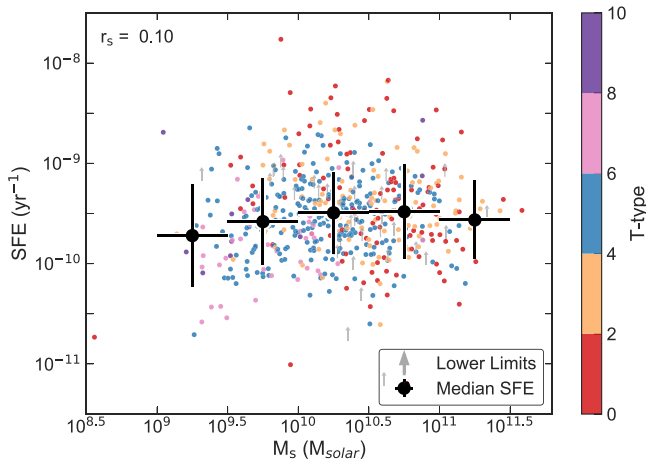


Figure 11. SFE and the stellar mass for the spiral sample. Median SFEs for each stellar mass bin are estimated including the H I mass upper limits for non-H I detections, and the SFE medians and 1σ values are listed in Table 7. For stellar masses ranging from 10^9 to $10^{11.5} M_\odot$, the SFE for spirals remains constant at a median value of $\log \text{SFE} = -9.57$ and 1σ spread of 0.4 dex. SFE appears to be almost constant with T-type and stellar mass, despite the fact that high-mass galaxies with T-type < 2 fall below the MS and may have commenced quenching.

Maddox et al. (2015) also measured the largest spin parameter to be $\lambda \sim 0.2$, confirming the upper limit on the halo spin parameter predicted by numerical N -body simulations of cold dark matter (Knebe & Power 2008). They concluded that the upper limit on the H I fraction is set by the upper limit of the halo spin parameter due to the empirical correlation between the halo spin parameter and the H I fraction.

Obreschkow et al. (2016) found that for isolated local disk galaxies the fraction of atomic gas, f_{atm} , is described by a stability model for flat exponential disks. To see if the observed upper limit to the H I fraction of the spiral sample can be explained by the upper limit of the halo spin parameter, we calculate the f_{atm} relationship for $\lambda \approx 0.112$, following the method outlined in Obreschkow et al. (2016). Though $\lambda \sim 0.2$ is the maximum spin of a spherical halo, we choose to calculate the f_{atm} at $\lambda \approx 0.112$ because 99% of galaxy halos are predicted to lie below $\lesssim 0.112$ (Bullock et al. 2001). We define

Table 7
 The Median SFE and 1σ Values of Each Stellar Mass Bin for the Spiral Sample Shown in Figure 11

$\log(M_*)$ (M_\odot)	Median $\log(\text{SFE})$ (yr^{-1})	1σ (dex)	N
9.25	-9.72	0.51	29
9.75	-9.58	0.43	128
10.25	-9.49	0.41	222
10.75	-9.48	0.47	164
11.25	-9.56	0.39	35

the fraction of atomic gas as

$$f_{\text{atm}} = \frac{1.35M_{\text{HI}}}{M}, \quad (12)$$

where M is the disk baryonic mass ($M = M_* + 1.35M_{\text{HI}}$) and the factor of 1.35 accounts for the universal helium fraction (Obreschkow et al. 2016). Obreschkow et al. (2016) models the rotation curve of spiral galaxies as

$$f_{\text{atm}} = \min \{1, 2.5q^{1.12}\}, \quad (13)$$

where q is the global stability parameter. This parameter is defined as:

$$q = \frac{j\sigma}{GM} = 0.22 \frac{\lambda}{0.03} \left(\frac{M}{10^9 M_\odot} \right)^{-1/3}, \quad (14)$$

where j is the baryonic specific angular momentum of the disk, σ is the velocity dispersion of the atomic gas and mass is in units of $10^9 M_\odot$. The global stability parameter is simplified by making two assumptions: first, that disk galaxies condense out of scale-free cold dark matter halos, and second, that $j \propto \lambda$ (Obreschkow & Glazebrook 2014; Obreschkow et al. 2016). Under these assumptions, Equation (13) simplifies to:

$$f_{\text{atm}} = \min \left\{ 1, 0.5 \left(\frac{\lambda}{0.03} \right)^{1.12} \left(\frac{M}{10^9 M_\odot} \right)^{-0.37} \right\}, \quad (15)$$

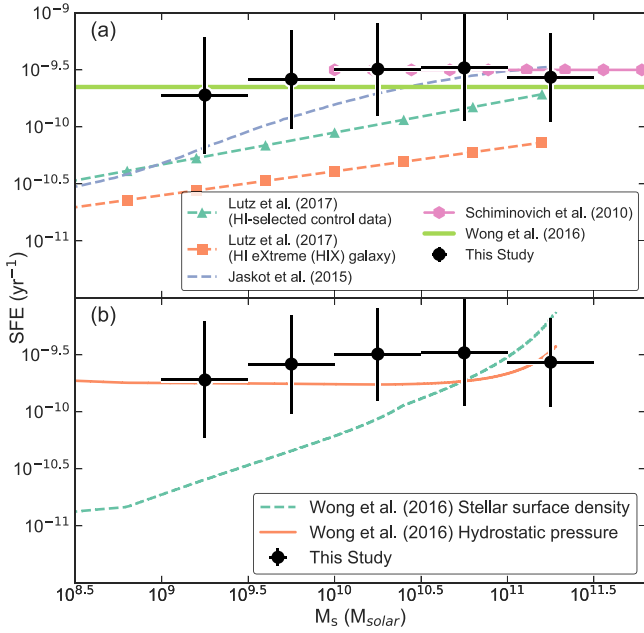


Figure 12. (Panel a) The median SFE and stellar mass for the spiral sample, alongside scaling relations observed in the prior literature (i.e., Schiminovich et al. 2010; Huang et al. 2012; Wong et al. 2016; Lutz et al. 2017) and (panel b) two models presented by Wong et al. (2016). HI-selected samples show that SFE increases with stellar mass, but this is an artifact of excluding low HI mass galaxies. Stellar mass-selected samples, on the other hand, show that SFE is constant with stellar mass, with normalization between $10^{-9.65}$ to $10^{-9.5} \text{ yr}^{-1}$. Of the two models presented by Wong et al. (2016), the hydrostatic pressure model provides the best agreement with our data.

and using Equation (12), this can be rearranged to give

$$\frac{M_{\text{HI}}}{10^9 M_{\odot}} = \min \left\{ \frac{M}{1.35 \times 10^9 M_{\odot}}, 18 \lambda^{1.12} \left(\frac{M}{10^9 M_{\odot}} \right)^{-0.63} \right\}. \quad (16)$$

Figure 13 illustrates the comparison between Equation (16) and the empirical HI–stellar mass distribution of the spiral sample. We also include the predicted f_{atm} curve for $\lambda \approx 0.03$, as this value of λ corresponds to the mode of the empirically measured halo spin parameter distribution (Bullock et al. 2001). The median bins of the spiral sample are in agreement with this prediction of f_{atm} , while the highest HI mass galaxies lie below the predicted upper limit for f_{atm} , when $\lambda = 0.112$. We find that the model of Obreschkow et al. (2016) matches well with the empirical data of the spiral sample, consistent with the hypothesis that the upper limit of the HI fraction is set by that of the halo spin parameter.

7.2. Why is SFE Constant?

We find that SFE is constant across two orders of magnitude of stellar mass, which agrees with the findings of Catinella et al. (2010) and Wong et al. (2016), while disagreeing with others (e.g., Huang et al. 2012; Lutz et al. 2017). Wong et al. (2016) tested two models for molecular gas content within galaxies: one where molecular gas is a function of stellar surface density and another where it is a function of hydrostatic pressure. The stellar surface density prescription (Leroy et al. 2008; Zheng

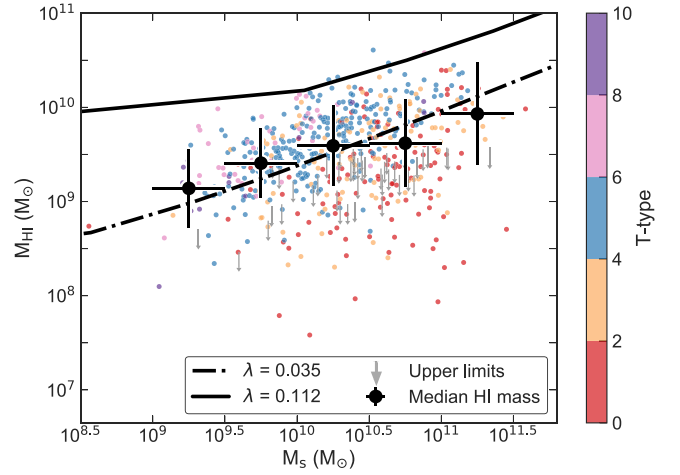


Figure 13. HI mass vs. stellar mass for the spiral sample. The solid and dashed black lines represent the model, Equation (16), for when $\lambda = 0.112$ and 0.035 , respectively. The median bins of the spiral sample are in good agreement with the model of Obreschkow et al. (2016), as they lie on the expected mean f_{atm} (for $\lambda = 0.035$). The upper HI masses of the spiral sample line up with the expected f_{atm} for $\lambda = 0.112$, and therefore the maximum HI mass for a given stellar mass is determined by the upper limit in the halo spin parameter.

et al. 2013) defines the molecular-to-atomic ratio, R_{mol} , as

$$R_{\text{mol},s} = \frac{\Sigma_{*}}{81 M_{\odot} \text{ pc}^{-1}}, \quad (17)$$

where Σ_{*} is the stellar surface density. The R_{mol} for the hydrostatic pressure prescription (Zheng et al. 2013) is defined as

$$R_{\text{mol},p} = \left(\frac{P_h}{1.7 \times 10^4 \text{ cm}^{-3} \text{ K } k_B} \right)^{0.8}, \quad (18)$$

where P_h is the hydrostatic pressure (Elmegreen 1989) and k_B is the Boltzmann constant.

Similarly to Wong et al. (2016), we find that the constant SFE can be described by a model of the marginally stable disk, while the hydrostatic pressure model provides a better prescription for estimating the SFE and molecular-to-atomic ratio. For massive galaxies with large optical disks, previous studies (e.g., Leroy et al. 2008; Wong et al. 2013) observed a correlation between R_{mol} and stellar surface density. The two models given by Equations (17) and (18) also predict similar R_{mol} and integrated SFE for high-mass galaxies (Wong et al. 2016). But for low mass galaxies, the stellar surface density prescription does not predict the observed SFE because this prescription is unable to convert the HI to molecular hydrogen, and underestimates the amount of molecular hydrogen in regions with low stellar surface densities. Therefore, this method underestimates the SFR and SFE in dwarf galaxies. While the stellar surface density model predicts that SFE will decrease for smaller stellar mass galaxies, the hydrostatic pressure model predicts a higher molecular hydrogen content for low mass galaxies, and therefore a constant SFE with stellar mass, agreeing with the empirical data.

We note that Obreschkow et al. (2016) predict that most of the baryons in dwarf galaxies are in the form of HI gas ($f_{\text{atm}} = 1$) and therefore have low SFE because these systems are inefficient at converting their HI gas to molecular gas. We do not observe a decrease in SFE because these galaxies are

below the stellar mass range probed in our spiral sample. Our lowest stellar mass bin of $10^{9.0}$ and $10^{9.5} M_{\odot}$ hints at a turnover for the low mass dwarf, as predicted by Obreschkow et al. (2016). Combining the next generation of HI survey, WALLABY, with 20 cm radio continuum from ASKAP, we will measure the HI properties and SFR of $\sim 600,000$ galaxies, including a large number of dwarf galaxies populating the low mass end of Figure 12. Observing these low stellar mass dwarfs will provide a more complete picture about HI content and how efficiently dwarfs convert HI to molecular gas.

8. Summary

We have measured the relationship between HI mass, stellar mass, and SFE by using HICAT, archival HI data, and new WISE photometry. For this work, we provide new WISE aperture photometry for 3831 out of 4315 sources of HICAT and created three samples, an HI-selected sample, a spiral sample, and an M_s sample. We find the following:

1. Sample selection and biases are critical when interpreting and comparing measured relationships between HI mass, stellar mass, and SFE. HI-selected samples often exclude HI-poor galaxies (unlike stellar mass-selected samples) resulting in measurements of high median HI masses and low median SFEs.
2. HI mass increases with stellar mass for the spiral sample with a power-law index of 0.34. Also, at a given stellar mass, HI mass increases with T-type and dispersion in HI masses narrows for individual T-types. For example, for the $10^{10} M_{\odot}$ to $10^{10.5} M_{\odot}$ stellar mass bin, the median HI mass and scatter is $10^{9.26} M_{\odot}$ and 0.59 dex for T-types 0 to 2 and the $10^{9.72} M_{\odot}$ and 0.31 dex for T-types 6 to 8.
3. HI mass is constant with stellar mass for the M_s sample. While HI mass increases with stellar mass for spiral galaxies, the fraction of elliptical galaxies with little HI gas also increases with stellar mass, producing the observed flat relation.
4. The observed upper limit to the HI–stellar mass distribution of the spiral sample is consistent with the predicted HI–stellar mass curve for the upper limit for the halo spin parameter ($\lambda = 0.112$). This is consistent with the hypothesis that the maximum HI fraction is set by that of the halo spin parameter.
5. For a subsample of the spiral sample with stellar mass $\leq 10^{10.5} M_{\odot}$, we measure the MS to be $\log \text{SFR} = 0.7 (\log M_* - 10) - 0.09$ with a 1σ scatter of 0.27 dex. We see evidence of mass quenching (e.g., Kauffmann et al. 2003) as the median SFR is constant for spiral galaxies with stellar masses $> 10^{10} M_{\odot}$.
6. For the spiral sample, SFE is constant ($= 10^{-9.57} \text{ yr}^{-1} \pm 0.44$ dex) for 2.5 orders of magnitude in stellar mass and agrees with comparable measurements of stellar mass-selected samples of galaxies (Catinella et al. 2010; Schiminovich et al. 2010). This result is in broad agreement with the hydrostatic pressure model (Wong et al. 2016).
7. SFE is constant as a function of T-type and is constant for spiral galaxies that show evidence of mass quenching.

We would like to thank M. Cluver, T. Dolley, A. Groszek, V. Kilborn, K. Lutz, N. Maddox, G. Meurer, D. Obreschkow, and I. Wong for the useful and insightful discussions.

This publication makes use of data products from the *Wide-field Infrared Survey Explorer*, which is a joint project of the University of California, Los Angeles, and the Jet Propulsion Laboratory/California Institute of Technology, funded by the National Aeronautics and Space Administration. This research has made use of the NASA/IPAC Extragalactic Database (NED) which is operated by the Jet Propulsion Laboratory, California Institute of Technology, under contract with the National Aeronautics and Space Administration and the HyperLeda database (<http://leda.univ-lyon1.fr>).

Appendix





Table 8 provides a full list of parameters of HICAT+WISE (HI-WISE) catalog that is available in machine-readable format.

Table 8
H I-*WISE* Parameter Descriptions

Parameter	Units	Description
Name		HIPASS designation
R.A.	deg	Right ascension (J2000)
Decl.	deg	Declination (J2000)
T-type		The T-type of galaxies reported by Bonne et al. (2015) or NED.
Dist	Mpc	Luminosity distance
Dist Source Flag		Source of the distance: 0. Cosmicflows-3 (Tully et al. 2016), 1. HICAT, 2. NED
Optical Match Type		Our category matching choice: 0. no optical counterpart, 1. position and velocity match, 2. position match.
$vel_{H\ I}$	km s^{-1}	The flux weighted velocity average between minimum and maximum profile velocity.
S_p	Jy	Peak flux density of profile
S_{int}	Jy km s^{-1}	Integrated flux of source (within region v_{lo} , v_{hi} and box size)
W1	mag	W1 isophotal magnitude
W1err	mag	W1 magnitude error
W2	mag	W2 isophotal magnitude
W2err	mag	W2 magnitude error
W3	mag	W3 “best” magnitude
W3err	mag	W3 magnitude error
W3f		W3 “best” photometry type: 0. isophotal, 10. total magnitude
W4	mag	W4 “best” magnitude
W4err	mag	W4 magnitude error
W4f		W4 “best” photometry type: 0. isophotal, 10. total magnitude
R1iso	arcsec	W1 1σ isophotal radius (semimajor axis)
R2iso	arcsec	W2 1σ isophotal radius or photometry aperture (semimajor axis)
R3iso	arcsec	W3 1σ isophotal radius or photometry aperture (semimajor axis)
R4iso	arcsec	W4 1σ isophotal radius or photometry aperture (semimajor axis)
ba		Axis ratio based on the W1 3σ isophote
pa	deg	Position angle (east of north) based on the W1 3σ isophote
W1W2	mag	W1–W2 color, where the W1 aperture is matched to the W2 1σ isophotal aperture
W1W2err	mag	W1–W2 color uncertainty
W2W3	mag	W2–W3 color, using the W2 isophotal aperture and the W3 isophotal aperture
W2W3err	mag	W2–W3 color uncertainty
W1–W2	mag	K-corrected (rest-frame) W1–W2 color
W2–W3	mag	K-corrected (rest-frame) W2–W3 color
$\log L_{W1}$	$\log L_{\odot}$	W1 νL_{ν} luminosity (log10)
$\log L_{W1}$ err	$\log L_{\odot}$	Uncertainty in $\log L_{W1}$
$\log L_{W2}$	$\log L_{\odot}$	W2 νL_{ν} luminosity (log10)
$\log L_{W2}$ err	$\log L_{\odot}$	Uncertainty in $\log L_{W2}$
$\log L_{W3}$	$\log L_{\odot}$	W3 νL_{ν} luminosity (log10). This includes the stellar continuum.
$\log L_{W3}$ err	$\log L_{\odot}$	Uncertainty in $\log L_{W3}$
$\log L_{W4}$	$\log L_{\odot}$	W4 νL_{ν} luminosity (log10). This includes the stellar continuum.
$\log L_{W4}$ err	$\log L_{\odot}$	Uncertainty in $\log L_{W4}$
$\log L_{W1}(L_{\odot})$	$\log L_{\odot}$	W1 in-band luminosity (log10)
$\log L_{W1}(L_{\odot})$ err	$\log L_{\odot}$	Uncertainty in $\log L_{W1}(L_{\odot})$
W1flux	mJy	WISE W1 K-corrected flux
W2flux	mJy	WISE W2 K-corrected flux
w3PaH	mJy	WISE W3 K-corrected flux, with the stellar continuum subtracted; result is the “PaH” flux
w4dust	mJy	WISE W4 K-corrected flux, with the stellar continuum subtracted; result is the warm dust flux
$\log M_*$	$\log(M_{\odot})$	Stellar mass (log10), based on the W1–W2 K-corrected color and the W1 in-band luminosity ($L_{W1}(L_{\odot})$) (Cluver et al. 2014).
$\log M_*$ err	$\log(M_{\odot})$	Uncertainty in $\log M_*$
$\log M_{H\ I}$	$\log(M_{\odot})$	H I mass (log10)
$\log M_{H\ I}$ err	$\log(M_{\odot})$	Uncertainty in $\log M_{H\ I}$
$\log \text{SFR}$	$\log(M_{\odot} \text{ yr}^{-1})$	Star formation rate (log10) based on the W3 νL_{ν} luminosity (Brown et al. 2017).
$\log \text{SFR}$ err	$\log(M_{\odot} \text{ yr}^{-1})$	Uncertainty in $\log \text{SFR}$
$\log \text{SFE}$	$\log(\text{yr}^{-1})$	Star formation efficiency (log10).
$\log \text{SFE}$ err	$\log(\text{yr}^{-1})$	Uncertainty in $\log \text{SFE}$

(This table is available in its entirety in machine-readable form.)

ORCID iDs

Vaishali Parkash  <https://orcid.org/0000-0003-3982-6304>
 Michael J. I. Brown  <https://orcid.org/0000-0002-1207-9137>
 T. H. Jarrett  <https://orcid.org/0000-0002-4939-734X>
 Nicolas J. Bonne  <https://orcid.org/0000-0001-9569-8808>

References

- Barnes, D. G., Staveley-Smith, L., de Blok, W. J. G., et al. 2001, *MNRAS*, **322**, 486
- Boissier, S., & Prantzos, N. 2000, *MNRAS*, **312**, 398
- Bolatto, A. D., Wolfire, M., & Leroy, A. K. 2013, *ARA&A*, **51**, 207
- Bonne, N. J., Brown, M. J. I., Jones, H., & Pimbblet, K. A. 2015, *ApJ*, **799**, 160
- Brinchmann, J., Charlot, S., White, S. D. M., et al. 2004, *MNRAS*, **351**, 1151
- Brown, M. J. I., Moustakas, J., Kennicutt, R. C., et al. 2017, *ApJ*, **847**, 136
- Bullock, J. S., Kolatt, T. S., Sigad, Y., et al. 2001, *MNRAS*, **321**, 559
- Calzetti, D., Kennicutt, R. C., Engelbracht, C. W., et al. 2007, *ApJ*, **666**, 870
- Catinella, B., Schiminovich, D., Cortese, L., et al. 2013, *MNRAS*, **436**, 34
- Catinella, B., Schiminovich, D., Kauffmann, G., et al. 2010, *MNRAS*, **403**, 683
- Catinella, B., Schiminovich, D., Kauffmann, G., et al. 2012, *A&A*, **544**, A65
- Chabrier, G. 2003, *PASP*, **115**, 763
- Chen, Y.-M., Wild, V., Kauffmann, G., et al. 2009, *MNRAS*, **393**, 406
- Cluver, M. E., Jarrett, T. H., Dale, D. A., et al. 2017, *ApJ*, **850**, 68
- Cluver, M. E., Jarrett, T. H., Hopkins, A. M., et al. 2014, *ApJ*, **782**, 90
- Cutri, R. M., Wright, E. L., Conrow, T., et al. 2013a, Explanatory Supplement to the WISE All-Sky Data Release Products, Tech. Rep. 1
- Cutri, R. M., Wright, E. L., Conrow, T., et al. 2013b, *yCat*, **2328**
- Doyle, M. T., & Drinkwater, M. J. 2006, *MNRAS*, **372**, 977
- Doyle, M. T., Drinkwater, M. J., Rohde, D. J., et al. 2005, *MNRAS*, **361**, 34
- Driver, S. P., Norberg, P., Baldry, I. K., et al. 2009, *A&G*, **50**, 5.12
- Elbaf, D., Daddi, E., Le Borgne, D., et al. 2007, *A&A*, **468**, 33
- Elmegreen, B. G. 1989, *ApJ*, **338**, 178
- Fixsen, D. J., Cheng, E. S., Gales, J. M., et al. 1996, *ApJ*, **473**, 576
- Gabor, J. M., Davé, R., Finlator, K., & Oppenheimer, B. D. 2010, *MNRAS*, **407**, 749
- Grootes, M. W., Tuffs, R. J., Popescu, C. C., et al. 2013, *ApJ*, **766**, 59
- Helou, G., Roussel, H., Appleton, P., et al. 2004, *ApJS*, **154**, 253
- Huang, S., Haynes, M. P., Giovanelli, R., & Brinchmann, J. 2012, *ApJ*, **756**, 113
- Huang, T.-C., Goto, T., Hashimoto, T., Oi, N., & Matsuhara, H. 2017, [arXiv:1712.01861](https://arxiv.org/abs/1712.01861)
- Huchtmeier, W. K., & Richter, O.-G. 1989, A General Catalog of HI Observations of Galaxies: The Reference Catalog (Berlin: Springer)
- Jarrett, T. H., Chester, T., Cutri, R., et al. 2000, *AJ*, **119**, 2498
- Jarrett, T. H., Cluver, M. E., Magoulas, C., et al. 2017, *ApJ*, **836**, 182
- Jarrett, T. H., Cohen, M., Masci, F., et al. 2011, *ApJ*, **735**, 112
- Jarrett, T. H., Masci, F., Tsai, C. W., et al. 2012, *AJ*, **144**, 68
- Jarrett, T. H., Masci, F., Tsai, C. W., et al. 2013, *AJ*, **145**, 6
- Jaskot, A. E., Oey, M. S., Salzer, J. J., et al. 2015, *ApJ*, **808**, 66
- Jones, D. H., Read, M. A., Saunders, W., et al. 2009, *MNRAS*, **399**, 683
- Kauffmann, G., Heckman, T. M., Tremonti, C., et al. 2003, *MNRAS*, **346**, 1055
- Kennicutt, R. C., Jr. 1998, *ARA&A*, **36**, 189
- Kereš, D., Katz, N., Fardal, M., Davé, R., & Weinberg, D. H. 2009, *MNRAS*, **395**, 160
- Knebe, A., & Power, C. 2008, *ApJ*, **678**, 621
- Leroy, A. K., Walter, F., Brinks, E., et al. 2008, *AJ*, **136**, 2782
- Lintott, C., Schawinski, K., Bamford, S., et al. 2011, *MNRAS*, **410**, 166
- Lintott, C. J., Schawinski, K., Slosar, A., et al. 2008, *MNRAS*, **389**, 1179
- Lutz, K. A., Kilborn, V. A., Catinella, B., et al. 2017, *MNRAS*, **467**, 1083
- Maddox, N., Hess, K. M., Obreschkow, D., Jarvis, M. J., & Blyth, S.-L. 2015, *MNRAS*, **447**, 1610
- Mainzer, A., Bauer, J., Cutri, R. M., et al. 2014, *ApJ*, **792**, 30
- Makarov, D., Prugniel, P., Terekhova, N., Courtois, H., & Vauglin, I. 2014, *A&A*, **570**, A13
- Masters, K. L., Crook, A., Hong, T., et al. 2014, *MNRAS*, **443**, 1044
- Meidt, S. E., Schinnerer, E., Knapen, J. H., et al. 2012, *ApJ*, **744**, 17
- Meidt, S. E., Schinnerer, E., van de Ven, G., et al. 2014, *ApJ*, **788**, 144
- Meyer, M. J., Zwaan, M. A., Webster, R. L., et al. 2004, *MNRAS*, **350**, 1195
- Mirabel, I. F., & Sanders, D. B. 1988, *ApJ*, **335**, 104
- Noeske, K. G., Weiner, B. J., Faber, S. M., et al. 2007, *ApJL*, **660**, L43
- Obreschkow, D., & Glazebrook, K. 2014, *ApJ*, **784**, 26
- Obreschkow, D., Glazebrook, K., Kilborn, V., & Lutz, K. 2016, *ApJL*, **824**, L26
- Oliver, S., Frost, M., Farrah, D., et al. 2010, *MNRAS*, **405**, 2279
- Patulel, G., Petit, C., Prugniel, P., et al. 2003, *A&A*, **412**, 45
- Ponomareva, A. A., Verheijen, M. A. W., Papastergis, E., Bosma, A., & Peletier, R. F. 2018, *MNRAS*, **474**, 4366
- Prochaska, J. X., & Wolfe, A. M. 2009, *ApJ*, **696**, 1543
- Rodighiero, G., Daddi, E., Baronchelli, I., et al. 2011, *ApJL*, **739**, L40
- Salim, S., Rich, R. M., Charlot, S., et al. 2007, *ApJS*, **173**, 267
- Schiminovich, D., Catinella, B., Kauffmann, G., et al. 2010, *MNRAS*, **408**, 919
- Schruba, A., Leroy, A. K., Walter, F., et al. 2011, *AJ*, **142**, 37
- Serra, P., Oosterloo, T., Morganti, R., et al. 2012, *MNRAS*, **422**, 1835
- Speagle, J. S., Steinhardt, C. L., Capak, P. L., & Silverman, J. D. 2014, *ApJS*, **214**, 15
- Springob, C. M., Haynes, M. P., Giovanelli, R., & Kent, B. R. 2005, *ApJS*, **160**, 149
- Stern, D., Assef, R. J., Benford, D. J., et al. 2012, *ApJ*, **753**, 30
- Taylor, E. N., Hopkins, A. M., Baldry, I. K., et al. 2011, *MNRAS*, **418**, 1587
- Tully, R. B., Courtois, H. M., & Sorce, J. G. 2016, *AJ*, **152**, 50
- Véron-Cetty, M.-P., & Véron, P. 2010, *A&A*, **518**, A10
- Wong, O. I., Meurer, G. R., Zheng, Z., et al. 2016, *MNRAS*, **460**, 1106
- Wong, T., Xue, R., Bolatto, A. D., et al. 2013, *ApJL*, **777**, L4
- Wright, E. L., Eisenhardt, P. R. M., Mainzer, A. K., et al. 2010, *AJ*, **140**, 1868
- Wuyts, S., Förster Schreiber, N. M., Lutz, D., et al. 2011, *ApJ*, **738**, 106
- York, D. G., Adelman, J., Anderson, J. E., et al. 2000, *AJ*, **120**, 1579
- Zahid, H. J., Dima, G. I., Kewley, L. J., Erb, D. K., & Davé, R. 2012, *ApJ*, **757**, 54
- Zheng, Z., Meurer, G. R., Heckman, T. M., Thilker, D. A., & Zwaan, M. A. 2013, *MNRAS*, **434**, 3389
- Zwaan, M. A., Meyer, M. J., Webster, R. L., et al. 2004, *MNRAS*, **350**, 1210